
On the influence of shock-cloud interactions on the nonthermal X-ray emission from the supernova remnant RCW 86

Aya BAMBA^{1,2,3}, Hidetoshi SANO⁴, Ryo YAMAZAKI^{5,6} and Jacco VINK⁷

¹Department of Physics, Graduate School of Science, The University of Tokyo, 7-3-1 Hongo, Bunkyo-ku, Tokyo 113-0033, Japan

²Research Center for the Early Universe, School of Science, The University of Tokyo, 7-3-1 Hongo, Bunkyo-ku, Tokyo 113-0033, Japan

³Trans-Scale Quantum Science Institute, The University of Tokyo, Tokyo 113-0033, Japan

⁴Faculty of Engineering, Gifu University, 1-1 Yanagido, Gifu 501-1193, Japan

⁵Department of Physical Sciences, Aoyama Gakuin University 5-10-1 Fuchinobe Chuo-ku, Sagami-hara, Kanagawa 252-5258, Japan

⁶Institute of Laser Engineering, Osaka University, 2-6 Yamadaoka, Suita, Osaka 565-0871, Japan

⁷Anton Pannekoek Institute for Astronomy & GRAPPA, University of Amsterdam, Science Park 904, 1098 XH Amsterdam, The Netherlands

*E-mail: bamba@phys.s.u-tokyo.ac.jp

Received ; Accepted

Abstract

It is an open issue how the surrounding environment of supernova remnant shocks affect non-thermal X-rays from accelerated electrons, with or without interacting dense material. We have conducted spatially resolved X-ray spectroscopy of the shock-cloud interacting region of RCW 86 with XMM-Newton. It is found that bright soft X-ray filaments surround the dense cloud observed with ^{12}CO and H_I emission lines. These filaments are brighter in thermal X-ray emission, and fainter and possibly softer in synchrotron X-rays, compared to those without interaction. Our results show that the shock decelerates due to the interaction with clouds, which results in an enhancement of thermal X-ray emission. This could possibly also explain the softer X-ray synchrotron component, because it implies that those shocks that move through a low density environment, and therefore decelerate much less, can be more efficient accelerators. This is similar to SN 1006 and Tycho, and is in contrast to RX J1713.7–3946. This difference among remnants may be due to the clumpiness of dense material interacting with the shock, which should be examined with future observations.

Key words: acceleration of particles — shock waves — ISM: individual objects (RCW 86) — cosmic rays — X-rays: ISM

1 Introduction

Shocks of supernova remnants (SNRs) are the most plausible site of Galactic cosmic ray acceleration. Together with X-ray observations, it is known that the magnetic field on the shocks is amplified and turbulent, which makes thin and bright synchrotron X-ray filaments or knots on the shock (Bell 2004; Bamba et al. 2003; Bamba et al. 2005; Vink & Laming 2003; Uchiyama et al. 2007, for example). One of the most important remaining problem is what kind of environment makes such a magnetic field amplification — when the maximum energy of accelerated electron is limited by synchrotron cooling, the maximum energy of accelerated electrons is proportional to the square of the shock velocity (e.g., Aharonian & Atoyan 1999; Yamazaki et al. 2006; Zirakashvili & Aharonian 2007), implying that the low density environment makes the maximum energy larger since the shock remains fast with a low deceleration. In fact, many synchrotron X-ray dominated SNRs emit no or only faint thermal X-ray emission was detected (Koyama et al. 1997; Slane et al. 2001; Bamba et al. 2001; Yamaguchi et al. 2004; Bamba et al. 2012). Lopez et al. (2015) made the spatially resolved spectroscopy of Tycho with NuSTAR, and showed that the high shock-speed regions have high energy cut-off of synchrotron X-rays. On the other hand, Inoue et al. (2009); Inoue et al. (2012) suggested that the shock-cloud interaction amplifies turbulent magnetic field. Such clumpy clouds also affect the GeV-TeV spectra from supernova remnants and X-ray variability (Celli et al. 2019). Sano et al. (2013) discovered some molecular cloud clumps in RX J1713.7–3946 surrounded by synchrotron X-ray filaments, and Sano et al. (2015) showed that the high interstellar gas density regions tend to have harder X-ray spectra in this remnant. These results confirm the scenario that a clumpy medium enhances turbulence and hence facilitates X-ray synchrotron emission. We need more samples to investigate what happens on the shock-cloud interacting regions in supernova remnants.

RCW 86 is one of the SNRs emitting synchrotron X-rays (Bamba et al. 2000; Borkowski et al. 2001a), GeV gamma-rays (Lemoine-Goumard et al. 2012; Yuan et al. 2014), and very high energy gamma-rays (H. E. S. S. Collaboration et al. 2018). An interesting characteristic of this SNR is that it emits not only synchrotron X-rays but also thermal X-rays, which makes this target unique among synchrotron X-ray dominated SNRs. The ratio of thermal and synchrotron X-rays in RCW 86 is different from position to position (Broersen et al. 2014; Tsubone et al. 2017), especially on the eastern rim (Vink et al. 2006), which can be due to the location dependence of shock wave velocity. The shock velocity measured by proper motion also changes rapidly especially on the eastern side (Yamaguchi et al. 2016). This can be connected to the fact that the south eastern part interacts with ^{12}CO and/or H I clouds (Sano et al. 2017; Sano et al. 2019). These facts make this SNR ideal to study the effect of shock-cloud interaction on the particle acceleration.

In this paper, we study the spatially resolved spectroscopy of RCW 86 shock-cloud interacting region, together with X-ray and the CO map comparisons, in order to understand how the interaction affects particle acceleration. Section 2 describes the data set as well as the data reduction. The imaging and spectral analysis results are described in section 3. Finally, we discuss our results in section 4. Throughout this paper, we adopt 2.3 kpc as the distance to our target (Sollerman et al. 2003; Helder et al. 2013).

2 Observations and Data reduction

The southeast region of RCW86 was observed with XMM-Newton (Jansen et al. 2001) on 2014 January 27. The data reduction and analysis was done with SAS version 20.0.0 (Gabriel et al. 2004). We selected only the data taken by the MOS cameras (Turner et al. 2001) since the MOS camera has a better energy resolution and a lower background level compared with the pn camera. We made the cleaned data with the standard method of XMM-Newton following the SAS guide, and the resultant exposure time is 101 ks. For the spectral analysis, we used xspec 12.12.1 in headas 6.30.1.

3 Results

3.1 Images

Figure 1 shows the MOS2 0.5–2.0 keV (red) and 2.0–8.0 keV (blue) image of the southeastern region of RCW 86. We did not use MOS1 for the image analysis since several chips are not in operation. The $^{12}\text{CO}(J=2-1)$ map is also overlaid with white contours. One can see that several X-ray filaments beautifully surrounds the molecular clouds within a scale of ~ 1 arcmin or ~ 0.7 pc at 2.3 kpc distance, as if these filaments are aware of the contour levels, a result already reported on in the original paper by Sano et al. (2017).

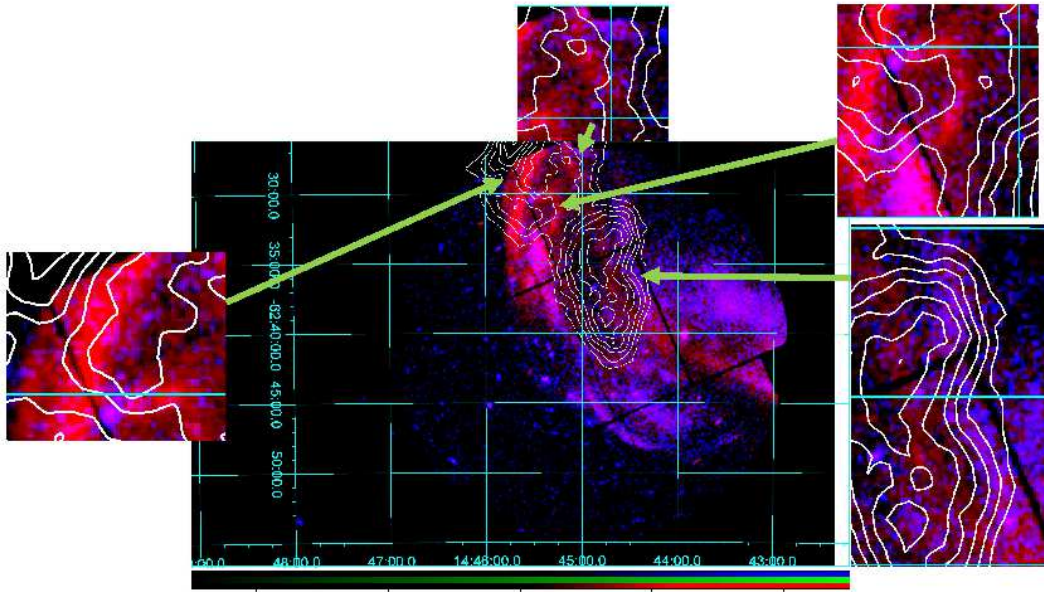


Fig. 1. MOS2 0.5–2.0 keV (red) and 2.0–8.0 keV (blue) band images of the southeastern region of RCW 86 in the logarithmic scales. The images are binned with 64×64 pixels. The vignetting correction and Non-X-ray-background subtraction is not performed. Color range is between 0.2–20 cnt per binned pixel for the 0.5–2.0 keV band, whereas 0.2–5 cnt per binned pixel. Coordinates are in J2000. White contours represent $^{12}\text{CO}(J=2-1)$ distribution in the velocity range of -36 to -34 km s^{-1} taken by NANTEN2 (see Fig. 6 of Sano et al. (2017)). Small panels are closed up view of bright filaments.

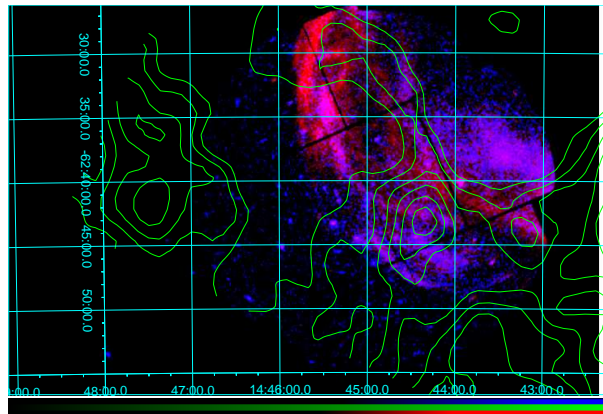


Fig. 2. Same MOS2 images to Figure 1, with H I distribution in the velocity range of -35 to -30 km s^{-1} taken by ATCA (Sano et al. 2017). The contours start from 45 K in the linear scale, with the interval of 2.5 K.

This result is already claimed by Sano et al. (2017). The filaments surrounding the molecular clouds look red, implying that their X-ray emission is softer than those from non-interacting regions.

One can see that there are soft X-ray filaments extending southwest beyond the molecular cloud. We thus examined whether there is dense material on these filaments in the the Australia Telescope Compact Array (ATCA) H I map taken by Sano et al. (2017). Figure 2 shows the same MOS2 map with H I contours. It is found that there is an associated H I cloud in the velocity range between -35 and -30 km s^{-1} , which is similar in range to the velocity of the ^{12}CO clouds that are associated with the SNR. The filaments are on the edge of the H I cloud, which is the same situation as the northern CO cloud cases.

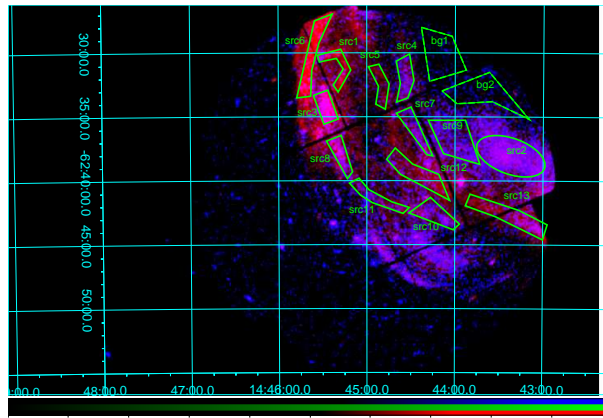


Fig. 3. Same MOS2 images to Figure 1, with source and background (solid and dashed, shown in green) regions for the spectral analysis.

3.2 Spectra

In order to examine the spectral difference among filaments, we selected thirteen regions for the spectral analysis, as shown in Fig. 3. The background regions were selected as the dashed regions. Since several regions are located outside of MOS1 field of view due to the lack of a CCD chip, we used only MOS2 camera data for such regions (src 1, 3, 4, 5, and 6).

Figure 4 show the background-subtracted spectrum for each region. One can see that some show softer spectra with emission lines, and other show harder spectra without lines. We thus fitted all spectra with a non-equilibrium thermal component (`nei` in `xspec`; Borkowski et al. 2001b) plus a power-law component to reproduce synchrotron X-rays. All the abundances are set to solar for the thermal emission. To represent the absorption model, we use the `phabs` model in XSPEC, which includes the cross sections of Balucinska-Church & McCammon (1992) with solar abundances (Anders & Grevesse 1989). We used Cash statistics for the spectral fitting (Cash 1979). The data are all well reproduced by these models, as shown in Table 1.

Ideally we would have preferred to take larger background regions in order to improve the statistics of the background spectra. There exist larger source-free regions that could, in principle, be used for background subtraction. However, we checked these regions and found that the non- X-ray background (NXB) and the Galactic Ridge X-ray Emission (GRXE) varies a lot from position to position, and these regions are, therefore, not suitable background spectra. In addition we checked blank-sky data in the same detector area as the source regions, but here the difficulty is that the blank-sky regions are from high Galactic latitude regions and do not correctly predict the GRXE component. For those reasons we prefer the less ideal background spectra taken from close to the source regions. Unfortunately, this does result in some residuals around the Si-K line band, most likely due to incorrectly taking into account the NXB components (src12 in Fig. 4 for example). Ignoring the Si-K line band for our fits produces slightly better fit statistics, but the best-fit parameters were not affected significantly excluding this band, and, in fact, for those spectra without large residuals around Si-K the fit statistics became even worse. So in the end we kept the Si-K band in our fit results. For src7 and 9, the spectra from MOS1 and MOS2 shows some normalization discrepancy. It can be due to the fact that these regions are near the edge of CCDs and the calibration uncertainty of normalization can be large. We thus made a simultaneous fit with coupled parameters but different normalization between MOS1 and MOS2 for src7 and 9 spectra. The best-fit normalization changed 20–30%, but still within the error region of the original fitting, because these regions are rather small and statistics are not so good. Thus, for simplicity, we adopted the same fitting method to other regions.

Figure 5 show the parameter maps of the spectral analysis result. The absorption column looks smaller on the cloud regions (see Fig. 5(a)), although it is not so obvious. Fig. 5(b) shows that the nonthermal component has larger photon index on the shock-cloud interacting regions (src1, 3, 5, 6, 11, 12, 13). These regions are bright in thermal X-rays (Fig. 5(f) but not so bright in nonthermal X-rays compared with non-interacting regions (Fig.5(e). Actually, the flux ratio between thermal and nonthermal emission changes two orders of magnitude as shown in Fig.5(g), implying that the interacting regions are really bright only in thermal X-rays. To illustrate this further, the panel (a) of Fig. 6 shows the scatter plot between the flux ratio and the photon index of nonthermal component. One can see that the photon

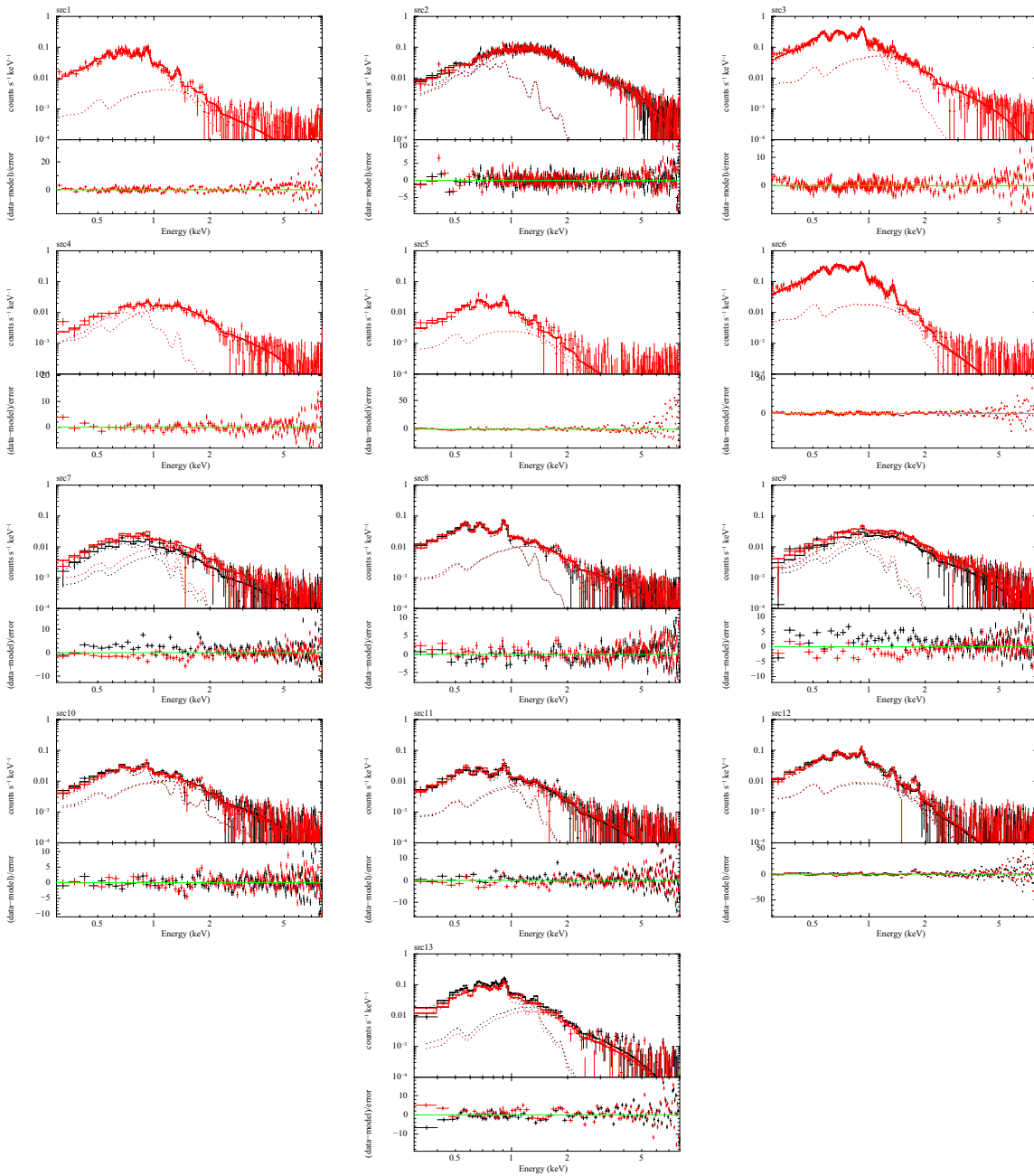


Fig. 4. Spatially resolved spectra with best-fit models. Black and red shows MOS1 and MOS2 data, respectively. The dotted lines represent *vnei* and power-law components. The data is binned for better visibility, whereas the fit is done without binning.

Table 1. Best-fit parameters for the spectral fitting.*

Reg.	Area (arcsec ²)	N_H (10 ²¹ cm ⁻²)	Γ	$F_{2-10\text{keV}}^\dagger$	kT_e (keV)	$n_e t$ (10 ¹⁰ s cm ⁻³)	Norm [§]	$F_{0.5-10\text{keV}}^\dagger$	C-stat./d.o.f.
src1	9349	4.1 (3.7–5.1)	3.11 (2.45–3.85)	0.17 (0.09–0.28)	0.43 (0.25–0.57)	1.4 (1.0–4.2)	30 (17–135)	23.5 (17.3–36.3)	1385.9/1533
src2	44411	5.5 (5.1–5.9)	2.84 (2.79–2.91)	1.54 (1.48–1.59)	—	—	7.5 (5.1–10.4)	4.5 (3.1–6.3)	3339.3/3074
src3	10373	4.6 (4.4–4.9)	3.31 (3.16–3.45)	0.28 (0.25–0.31)	0.34 (0.27–0.39)	1.6 (1.3–2.2)	36 (25–45)	20.9 (17.3–25.4)	1736.3/1533
src4	12114	5.6 (3.6–6.8)	3.25 (2.85–3.49)	0.41 (0.35–0.47)	0.24 (0.18–4.78)	6.2 (0.4–28.6)	16 (0.9–72)	4.8 (0.7–12.1)	1408.3/1533
src5	9902	4.3 (3.7–5.2)	4.16 (3.38–5.07)	0.02 (0.008–0.05)	0.66 (0.29–1.01)	0.7 (0.5–2.2)	4.4 (2.5–17.0)	5.0 (3.4–10.3)	1269.9/1533
src6	18934	4.5 (4.1–4.7)	4.49 (4.10–4.85)	0.14 (0.06–0.18)	0.34 (0.32–0.45)	2.0 (1.3–2.3)	171 (94–190)	104.0 (76.9–108.9)	1564.0/1533
src7	11448	4.6 (3.6–5.5)	2.83 (2.58–3.07)	0.32 (0.28–0.37)	0.35 (0.24–0.95)	2.1 (0.8–6.3)	7.3 (1.5–28)	4.6 (2.2–8.9)	3042.2/3072
src8	10301	4.8 (4.1–5.9)	2.86 (2.69–3.09)	0.38 (0.33–0.43)	0.24 (0.18–0.35)	2.5 (1.1–10.6)	57 (19–240)	18.8 (10.8–38.2)	3103.2/3072
src9	28590	5.4 (4.5–6.4)	2.92 (2.74–3.10)	1.22 (1.11–1.34)	0.34 (0.22–0.75)	2.2 (0.7–11.4)	15 (3.4–73)	9.1 (4.0–19.9)	3384.6/3072
src10	14664	3.8 (3.4–4.4)	2.85 (2.63–3.11)	0.39 (0.31–0.49)	1.88 (0.35–3.53)	0.42 (0.36–0.96)	2.6 (1.9–6.4)	4.4 (3.4–19.8)	2981.6/3072
src11	11786	5.5 (4.9–6.4)	3.50 (3.24–3.71)	0.13 (0.11–0.16)	0.21 (0.17–0.28)	4.1 (1.8–16.3)	50 (18–163)	11.9 (7.1–21.6)	3316.4/3078
src12	21340	4.0 (3.7–4.4)	4.13 (3.79–4.65)	0.043 (0.02–0.06)	0.69 (0.61–1.01)	0.8 (0.6–1.0)	6.8 (4.7–9.4)	8.0 (6.3–9.6)	3076.3/3072
src13	26501	6.4 (6.2–6.6)	3.36 (3.17–3.55)	0.50 (0.43–0.57)	0.20 (0.19–0.22)	14.1 (9.1–21.8)	417 (284–512)	85.9 (76.5–99.1)	2917.9/3078

* The errors are the 90% confidence level.

† 2–10 keV flux of the power-law component in the unit of 10⁻¹² erg cm⁻² s⁻¹.

‡ $\frac{10^{-18}}{4\pi D^2} \int n_e n_H dV$, where D , n_e , and n_H is the angular diameter distance to the source (cm), electron and hydrogen density (cm⁻³), respectively.

§ 0.5–10 keV flux of the thermal component in the unit of 10⁻¹² erg cm⁻² s⁻¹.

|| Fixed to the parameters for src9.

index is larger—i.e. the nonthermal spectrum is softer—in the regions where the thermal X-rays are dominant. Ideally we would like to compare the molecular-cloud densities with the X-ray parameters directly. However, the X-ray emission enhancement is on the edge of the molecular cloud, not on the center, which is difficult to see in the correlation plot. It is also unknown whether the cloud is physically interacts with the shock or not.

On the other hand, the thermal parameters, kT (Fig. 5(c)) and nt (Fig. 5(d)), show no clear tendency on the correlation with dense clouds. The correlation plot shown in the panel (b)–(d) of Fig. 6 also support no clear correlation.

4 Discussion

We carried out the spatially resolved spectroscopy and found that filaments interacting with the dense cloud have enhanced thermal emission, and fainter and possibly softer synchrotron X-rays. The absorption column on the cloud regions is rather small, which may imply that the cloud is on the rear side of the remnant.

The apparent positive correlation between the flux ratio of thermal and nonthermal X-rays and the photon index of nonthermal X-rays shown in Figure 6(a) can be mainly due to a deceleration of the shock velocity caused by the interaction of the shock with dense material. In the synchrotron loss-limit regime, the roll-off energy of the synchrotron X-rays is proportional to the square of shock velocity (Aharonian & Atoyan 1999; Yamazaki et al. 2006; Zirakashvili & Aharonian 2007). Thus the interacting shocks should have smaller shock velocity, and softer (and as a result fainter) synchrotron X-rays. The thermal X-rays are enhanced by the shock compression, which results in bright soft X-ray filaments around

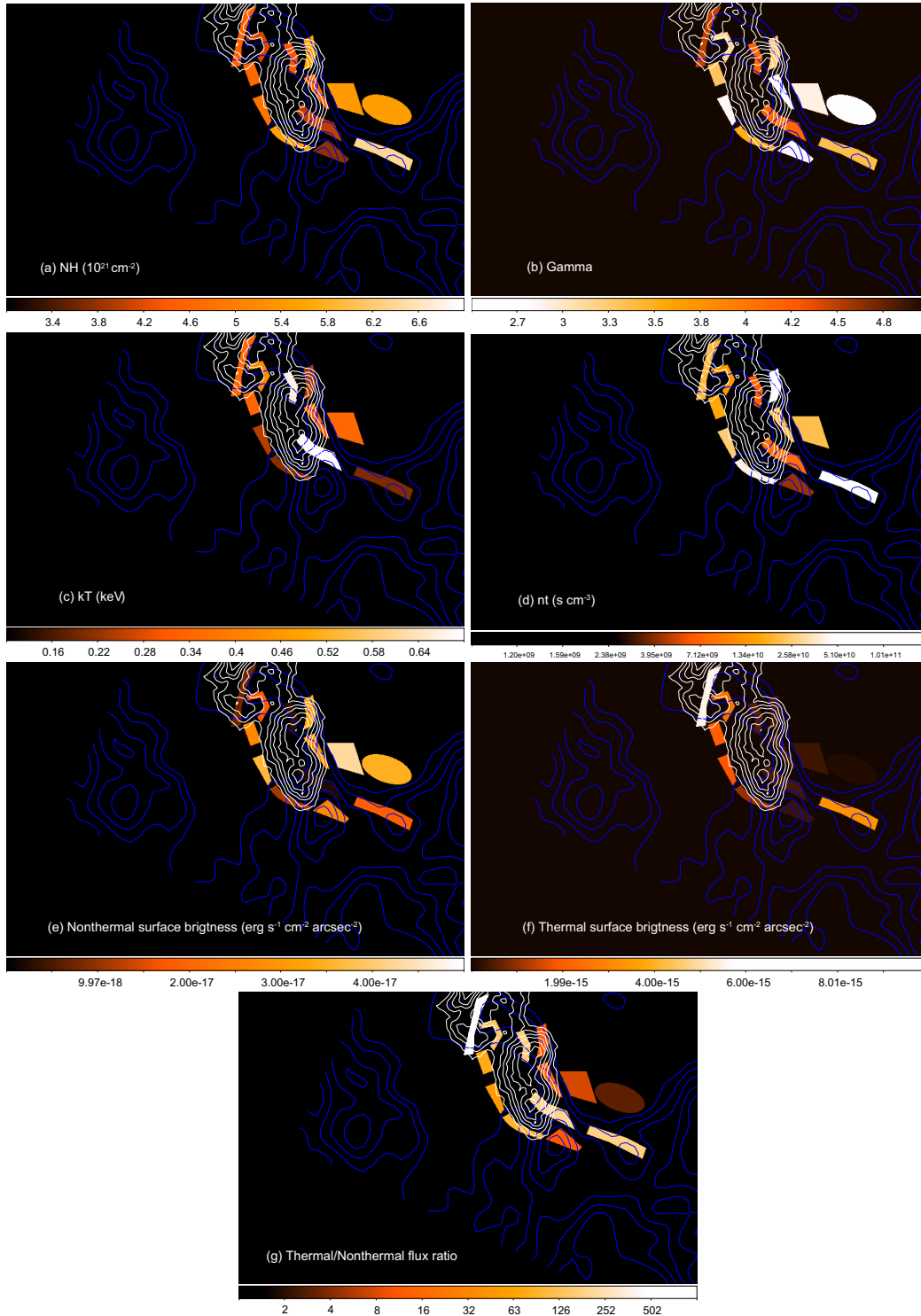


Fig. 5. Parameter maps of the spectral fitting, (a) absorption column, (b) photon index, (c) temperature, (d) ionization timescale, (e) nonthermal X-ray surface brightness in the 2–10 keV band in the unit of $\text{erg s}^{-1}\text{cm}^{-2}\text{arcsec}^{-2}$, (f) thermal X-ray surface brightness in the 0.5–10 keV band in the unit of $\text{erg s}^{-1}\text{cm}^{-2}\text{arcsec}^{-2}$, and (g) flux ratio between thermal and nonthermal emission. Color scales are in linear for (a), (b), and (c), (e), and (f), whereas in logarithmic for (d) and (g). For (c) and (d), We have no data for src2 region. White and blue contours represents ^{12}CO and H I distribution, same as Fig 1 and Fig 2, respectively.

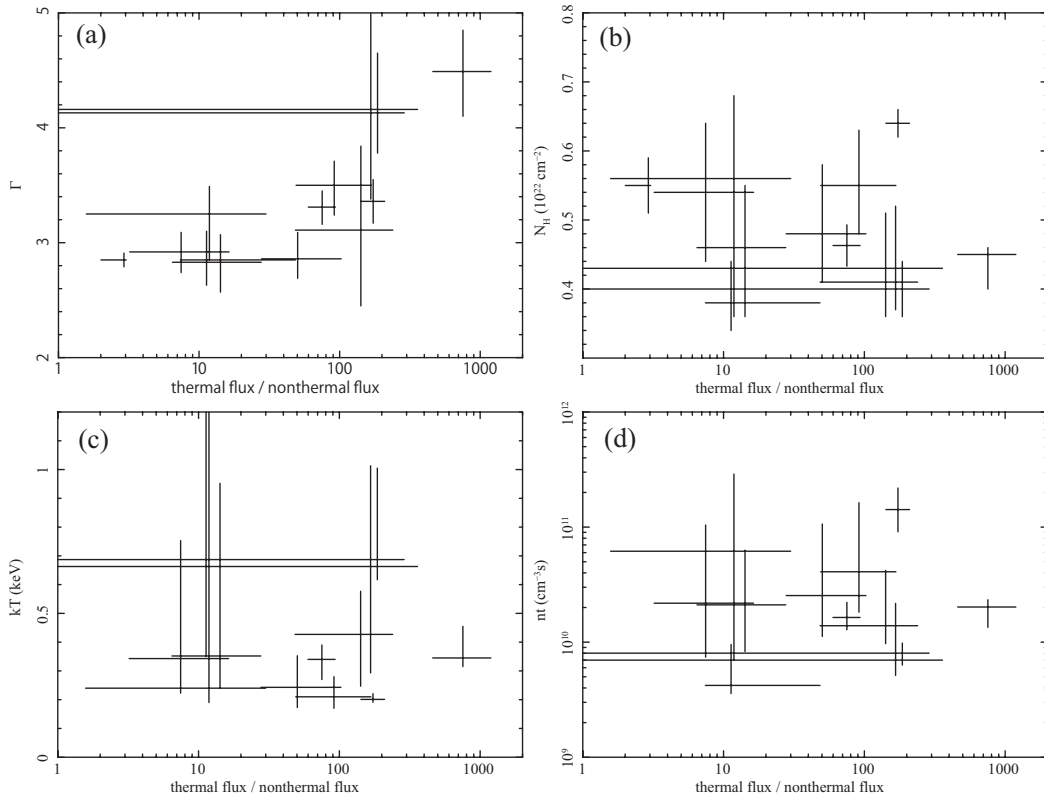


Fig. 6. Correlation plot between the flux ratio of the thermal and nonthermal components and the photon index of nonthermal emission (a), N_{H} (b), kT_e (c), and n_{et} (d).

the clouds. We thus conclude that this region of RCW 86 well follows the synchrotron loss-limit regime.

The enhancement of thermal X-rays, fainter and softer synchrotron X-ray emission is also shown in the interacting regions of several SNRs, such as the northwestern rim (Sano et al. 2022; Bamba et al. 2008) of SN 1006 and Tycho (Lopez et al. 2015). In most SNRs bright X-ray synchrotron emission appears also to coincide with no or very faint thermal X-ray emission (for example, Nakamura et al. 2012). These facts all imply that the bright synchrotron X-rays are emitted around non-interacting, fast shocks. Our results on RCW86 shows such a thermal X-ray enhancement and decline of synchrotron X-rays in the interacting regions with smaller spatial scales, 1 arcmin or 0.7 pc at 2.3 kpc distance, compared with previous results with the spatial scales of larger than a few pc.

On the other hand, our result is in contrast to the case of RX J1713.7–3946 (Sano et al. 2013), where synchrotron X-rays are enhanced around the shock-cloud interacting regions. Similarity to RX J1713–3946 is also observed in Kepler; Sapienza et al. (2022) revealed that the acceleration efficiency in the Kepler is higher in the north, interacting region with the shock and circumstellar medium, compared with the south of the remnant. Even in the same remnant, RCW 86, Suzuki et al. (2022) showed that thermal and synchrotron X-rays are enhanced in the denser region. Inoue et al. (2012) suggest that such a tendency happens on shocks colliding with clumpy clouds; when the shock runs into clumpy medium, the dense clumps can survive in the shock downstream region without evaporation and amplify the downstream magnetic field, which makes enhanced synchrotron X-rays (see also Sano & Fukui 2021).

This scenario may indicate that the difference between the shock-cloud interacting region in RCW86 and RX J1713.7–3946 can be the difference of environment of the shock. In RX J1713.7–3946 case, the inter-cloud density is $\sim 0.01\text{--}0.1\text{ cm}^{-3}$ (Weaver et al. 1977; Cassam-Chenai et al. 2004; Katsuda et al. 2015). Sano et al. (2020) discovered shocked cloudlets with the density of $\sim 10^4\text{ cm}^{-3}$, thus the clumpiness, the density contrast between dense cloud and inter-cloud regions, should be high. This is consistent with the calculation by Celli et al. (2019). On the other hand,

the density contrast between clouds and inter-cloud medium surrounding RCW86's eastern region can be smaller, since the dense cloud detected in ^{12}CO is covered by less-dense inter-cloud, which is detected with H I emission. The cloud interacting with SN 1006 is also detected by H I observation only (Sano et al. 2022), implying a less clumpy interstellar medium. Similar discussion is also done in Sano & Fukui (2021). On the interaction between the shock and such dense and rather uniform clouds, the shock-heated plasma can emit strong thermal bremsstrahlung, which should be the bright thermal filaments we observed. In order to test our scenario, we need high spatial resolution CO and H I observations of RCW86 to compare southwest (RX J1713-like) and eastern (SN 1006 like) regions to see if there are high density clouds and if density contrast makes the synchrotron X-ray enhancement.

In this study, we found no significant variation of temperature and ionization time scale of thermal emission. This is mainly due to the lack of energy resolution and statistics which lead large error ranges. Future X-ray missions with excellent energy resolution, such as XRISM (Tashiro et al. 2020) and Athena (Nandra et al. 2013), will resolve this issue.

5 Summary

The spatially resolved spectroscopy of the southeastern region of the young supernova remnant RCW86 is done with deep XMM-Newton observation. It is found that soft thermal X-rays are enhanced on the edge of dense clouds which is detected with ^{12}CO or H I observations. These regions show fainter and possibly softer nonthermal X-rays from accelerated electrons. These results indicate that the shock decelerate due to the interaction with clouds, which makes thermal X-ray enhancement due to the density increase and fainter and softer synchrotron X-rays due to smaller shock speed. Our results indicate that the dense region does not enhance synchrotron X-rays, in agreement with the suggestions by Aharonian & Atoyan (1999); Yamazaki et al. (2006); Zirakashvili & Aharonian (2007). No synchrotron X-ray enhancement on the shock-cloud interaction region is found in this region. This is similar to SN 1006 and Tycho, and contrastive to RX J1713.7–3946. This difference can be due to the difference of the surrounding environment, such as high density contrast of surrounding material. For further study of the effect of surrounding material to the synchrotron X-ray enhancement, we need follow-up observations with ALMA to study the density contrast of surrounding material of RCW86, and XRISM/Athena observations to measure precise parameters of thermal emission to understand the thermal conditions.

Acknowledgments

We thank the anonymous referee for his/her productive comments. We thank Hiromichi Okon and Yukikatsu Terada who helped us to make the parameter maps. This work was financially supported by Japan Society for the Promotion of Science Grants-in-Aid for Scientific Research (KAKENHI) Grant Numbers, JP19K03908 (AB), JP23H01211 (AB), 20KK0309 (HS), 21H01136 (HS), 22H01251 (RY), and 23H04899 (RY).

References

- Aharonian, F. A. & Atoyan, A. M. 1999, *A&A*, 351, 330. doi:10.48550/arXiv.astro-ph/9911158
- Anders, E. & Grevesse, N. 1989, *Geochim. Cosmochim. Acta*, 53, 197. doi:10.1016/0016-7037(89)90286-X
- Balucinska-Church, M. & McCammon, D. 1992, *ApJ*, 400, 699. doi:10.1086/172032
- Bamba, A., Koyama, K., & Tomida, H. 2000, *PASJ*, 52, 1157. doi:10.1093/pasj/52.6.1157
- Bamba, A., Ueno, M., Koyama, K., et al. 2001, *PASJ*, 53, L21. doi:10.1093/pasj/53.4.L21
- Bamba, A., Yamazaki, R., Ueno, M., et al. 2003, *ApJ*, 589, 827. doi:10.1086/374687
- Bamba, A., Yamazaki, R., Yoshida, T., et al. 2005, *ApJ*, 621, 793. doi:10.1086/427620
- Bamba, A., Fukazawa, Y., Hiraga, J. S., et al. 2008, *PASJ*, 60, S153. doi:10.1093/pasj/60.sp1.S153
- Bamba, A., Pühlhofer, G., Acero, F., et al. 2012, *ApJ*, 756, 149. doi:10.1088/0004-637X/756/2/149
- Bell, A. R. 2004, *MNRAS*, 353, 550. doi:10.1111/j.1365-2966.2004.08097.x
- Borkowski, K. J., Rho, J., Reynolds, S. P., et al. 2001, *ApJ*, 550, 334. doi:10.1086/319716
- Borkowski, K. J., Lyerly, W. J., & Reynolds, S. P. 2001, *ApJ*, 548, 820. doi:10.1086/319011
- Broersen, S., Chiotellis, A., Vink, J., et al. 2014, *MNRAS*, 441, 3040. doi:10.1093/mnras/stu667
- Cash, W. 1979, *ApJ*, 228, 939. doi:10.1086/156922
- Celli, S., Morlino, G., Gabici, S., et al. 2019, *MNRAS*, 487, 3199. doi:10.1093/mnras/stz1425
- Cassam-Chenai, G., Decourchelle, A., Ballet, J., et al. 2004, *A&A*, 427, 199. doi:10.1051/0004-6361:20041154
- Gabriel, C., Denby, M., Fyfe, D. J., et al. 2004, *Astronomical Data Analysis Software and Systems (ADASS) XIII*, 314, 759
- Helder, E. A., Vink, J., Bamba, A., et al. 2013, *MNRAS*, 435,

910. doi:10.1093/mnras/stt993
- H. E. S. S. Collaboration, Abramowski, A., Aharonian, F., et al. 2018, *A&A*, 612, A4. doi:10.1051/0004-6361/201526545
- Inoue, T., Yamazaki, R., & Inutsuka, S.-. ichiro . 2009, *ApJ*, 695, 825. doi:10.1088/0004-637X/695/2/825
- Inoue, T., Yamazaki, R., Inutsuka, S., et al. 2012, *ApJ*, 744, 71. doi:10.1088/0004-637X/744/1/71
- Jansen, F., Lumb, D., Altieri, B., et al. 2001, *A&A*, 365, L1. doi:10.1051/0004-6361:20000036
- Katsuda, S., Acero, F., Tominaga, N., et al. 2015, *ApJ*, 814, 29. doi:10.1088/0004-637X/814/1/29
- Koyama, K., Kinugasa, K., Matsuzaki, K., et al. 1997, *PASJ*, 49, L7. doi:10.1093/pasj/49.3.L7
- Lemoine-Goumard, M., Renaud, M., Vink, J., et al. 2012, *A&A*, 545, A28. doi:10.1051/0004-6361/201219896
- Lopez, L. A., Grefenstette, B. W., Reynolds, S. P., et al. 2015, *ApJ*, 814, 132. doi:10.1088/0004-637X/814/2/132
- Nakamura, R., Bamba, A., Dotani, T., et al. 2012, *ApJ*, 746, 134. doi:10.1088/0004-637X/746/2/134
- Nandra, K., Barret, D., Barcons, X., et al. 2013, arXiv:1306.2307. doi:10.48550/arXiv.1306.2307
- Sano, H., Tanaka, T., Torii, K., et al. 2013, *ApJ*, 778, 59. doi:10.1088/0004-637X/778/1/59
- Sano, H., Fukuda, T., Yoshiike, S., et al. 2015, *ApJ*, 799, 175. doi:10.1088/0004-637X/799/2/175
- Sano, H., Reynoso, E. M., Mitsuishi, I., et al. 2017, *Journal of High Energy Astrophysics*, 15, 1. doi:10.1016/j.jheap.2017.04.002
- Sano, H., Rowell, G., Reynoso, E. M., et al. 2019, *ApJ*, 876, 37. doi:10.3847/1538-4357/ab108f
- Sano, H., Inoue, T., Tokuda, K., et al. 2020, *ApJL*, 904, L24. doi:10.3847/2041-8213/abc884
- Sano, H. & Fukui, Y. 2021, *Ap&SS*, 366, 58. doi:10.1007/s10509-021-03960-4
- Sano, H., Yamaguchi, H., Aruga, M., et al. 2022, *ApJ*, 933, 157. doi:10.3847/1538-4357/ac7465
- Sapienza, V., Miceli, M., Bamba, A., et al. 2022, *ApJ*, 935, 152. doi:10.3847/1538-4357/ac8160
- Sollerman, J., Ghavamian, P., Lundqvist, P., et al. 2003, *A&A*, 407, 249. doi:10.1051/0004-6361:20030839
- Slane, P., Hughes, J. P., Edgar, R. J., et al. 2001, *ApJ*, 548, 814. doi:10.1086/319033
- Suzuki, H., Katsuda, S., Tanaka, T., et al. 2022, *ApJ*, 938, 59. doi:10.3847/1538-4357/ac8df7
- Tashiro, M., Maejima, H., Toda, K., et al. 2020, *Proc. SPIE*, 11444, 1144422. doi:10.1117/12.2565812
- Tsubone, Y., Sawada, M., Bamba, A., et al. 2017, *ApJ*, 835, 34. doi:10.3847/1538-4357/835/1/34
- Turner, M. J. L., Abbey, A., Arnaud, M., et al. 2001, *A&A*, 365, L27. doi:10.1051/0004-6361:20000087
- Uchiyama, Y., Aharonian, F. A., Tanaka, T., et al. 2007, *Nature*, 449, 576. doi:10.1038/nature06210
- Vink, J. & Laming, J. M. 2003, *ApJ*, 584, 758. doi:10.1086/345832
- Vink, J., Bleeker, J., van der Heyden, K., et al. 2006, *ApJL*, 648, L33. doi:10.1086/507628
- Weaver, R., McCray, R., Castor, J., et al. 1977, *ApJ*, 218, 377. doi:10.1086/155692
- Winkler, P. F., Williams, B. J., Reynolds, S. P., et al. 2014, *ApJ*, 781, 65. doi:10.1088/0004-637X/781/2/65
- Yamaguchi, H., Ueno, M., Koyama, K., et al. 2004, *PASJ*, 56, 1059. doi:10.1093/pasj/56.6.1059
- Yamaguchi, H., Katsuda, S., Castro, D., et al. 2016, *ApJL*, 820, L3. doi:10.3847/2041-8205/820/1/L3
- Yamazaki, R., Kohri, K., Bamba, A., et al. 2006, *MNRAS*, 371, 1975. doi:10.1111/j.1365-2966.2006.10832.x
- Yuan, Q., Huang, X., Liu, S., et al. 2014, *ApJL*, 785, L22. doi:10.1088/2041-8205/785/2/L22
- Zirakashvili, V. N. & Aharonian, F. 2007, *A&A*, 465, 695. doi:10.1051/0004-6361:20066494